Applied Numerical Mathematics 9 (1992) 45–71
North-Holland

High-order ENO schemes applied to two- and three-dimensional compressible flow

Chi-Wang Shu *
Division of Applied Mathematics, Brown University, Providence, RI 02912, USA

Thomas A. Zang
Theoretical Flow Physics Branch, NASA Langley Research Center, Hampton, VA 23665, USA

Gordon Erlebacher **
I.C.A.S.E., NASA Langley Research Center, Hampton, VA 23665, USA

David Whitaker
Computational Aerodynamics Branch, NASA Langley Research Center, Hampton, VA 23665, USA

Stanley Osher †
Department of Mathematics, University of California, Los Angeles, CA 90024, USA

Abstract

Shu, C.-W., T.A. Zang, G. Erlebacher, D. Whitaker and S. Osher, High-order ENO schemes applied to two- and three-dimensional compressible flow, Applied Numerical Mathematics 9 (1992) 45–71.

High-order essentially non-oscillatory (ENO) finite-difference schemes are applied to the two- and three-dimensional compressible Euler and Navier–Stokes equations. Practical issues, such as vectorization, efficiency of coding, cost comparison with other numerical methods and accuracy degeneracy effects, are discussed. Numerical examples are provided which are representative of computational problems of current interest in transition and turbulence physics. These require both non-oscillatory shock capturing and high resolution for detailed structures in the smooth regions and demonstrate the advantage of ENO schemes.

1. Introduction

In the computation of inviscid, compressible flow, the presence of infinitesimally thin shocks readily leads to nonlinear instability for traditional, unadulterated, linearly stable high-order methods. Moreover, regions of strong gradients which have finite thickness but are too thin for

* Research supported by NASA Contract #NAS1-18605 while in residence at ICASE, and by NSF Grant DMS 88-10150, NASA Langley Grant NAG1-1145 and AFOSR Grant 90-0093.
** Research supported by NASA Contract #NAS1-18605 while in residence at ICASE.
† Research supported by NSF Grant DMS 88-11863, DARPA Grant in the ACMP program, ONR Grant N00014-86-K-0691, NASA Langley Grant NAG 1-270, and NASA Contract #NAS1-18605 while in residence at ICASE.

the grid to resolve may also produce nonlinear instability. This is the case, for example, for high Reynolds number Navier–Stokes computations in which the shock thickness is much smaller than the grid spacing. The standard "cures" are either to add explicit artificial viscosity to the numerical method or to employ an upwind-biased scheme (which contains implicit artificial viscosity). Such approaches usually have the undesirable side effect of loss of resolution, particularly for the small-scale structures in the smooth part of the solution. The small-scale features are typically strongly and erroneously *damped* by the artificial viscosity. This problem even afflicts the formally high-order TVD (total-variation-diminishing) schemes, since they must degenerate to first-order accuracy at smooth critical points [13]. Certainly, the most difficult feature to capture is the passage of small-scale features through shock waves.

In many applications, such as typical steady-state aerodynamic CFD, the side effects of the artificial viscosity are not particularly worrisome since the main target of the computation is the large-scale flow structure and the details of the flow near the shock are not too significant. This is decidedly not the case, however, for numerical simulations of transition and turbulence. Here the interesting physical phenomena occur on scales much smaller than those of the mean flow. As noted by Hussaini and Zang [9], for incompressible flow spectral methods have been preferred for these applications since they have the best fidelity for the small-scale flow features. However, due to their extreme sensitivity to nonlinear instability, spectral methods have yet to be used for serious investigations of transition and turbulence in compressible flow with regions of strong gradients. (They can be used, of course, for shock-free flows [4] and for low Reynolds number viscous flows [5] in which thick shocks are actually *resolved* rather than *captured*.)

Essentially non-oscillatory (ENO) schemes, first introduced by Harten and Osher [6] and Harten et al. [7], can achieve uniformly high-order accuracy with sharp, essentially non-oscillatory shock transitions. The key idea is an adaptive stencil interpolation (based on difference tables) which automatically interpolates in a locally smoothest region. This strategy provides a strong inhibition towards differencing across discontinuities. In [22,23], Shu and Osher introduced an efficient implementation of ENO schemes, using the same adaptive stencil idea but working directly on fluxes and a special class of TVD high-order Runge–Kutta type time discretizations. It bypasses the reconstruction and Lax–Wendroff procedures in the original ENO schemes. For multi-dimensions, this simplification is significant, because the reconstruction in multi-dimensions becomes quite complicated [8]. Numerical examples in [22,23], especially the examples of shock interaction with entropy and vorticity waves, for which a good resolution for the detailed structures in the smooth region is as important as a sharp, non-oscillatory shock transition, indicate a good potential for ENO schemes in computing compressible Euler and Navier–Stokes equations.

In this paper, we discuss the coding of ENO schemes in [22,23] to two-dimensional general geometry (via transformation) and to three-dimensional Euler and Navier–Stokes equations of compressible gas dynamics on Cray X-MP and Y-MP. We address the practical issues such as vectorization, efficiency of evaluating Newton interpolations, cost comparison with other numerical methods, and accuracy degeneracy effects. We then present numerical examples which all require non-oscillatory shock capturing and high resolution for rich structures in the smooth regions, including two-dimensional shear flows, two-dimensional and three-dimensional homogeneous turbulence, and two-dimensional shock interaction with entropy and vorticity waves.

2. The Navier–Stokes and Euler equations

For completeness, we document here the three-dimensional, compressible Navier–Stokes equations as well as the various transformations that are required for the ENO method in curvilinear coordinates. In terms of the density ρ, the velocity $\hat{u} = (u, v, w)^t$, the pressure p, and the internal energy E, the Navier–Stokes equations read

$$\vec{q}_t + \vec{f}(\vec{q})_x + \vec{g}(\vec{q})_y + \vec{h}(\vec{q})_z = \vec{r}(\vec{q})_x + \vec{s}(\vec{q})_y + \vec{t}(\vec{q})_z, \tag{1}$$

where

$$\begin{aligned} &\vec{q} = (\rho, \rho u, \rho v, \rho w, E)^t, && \vec{f}(\vec{q}) = u\vec{q} + p(0, 1, 0, 0, u)^t, \\ &\vec{g}(\vec{q}) = v\vec{q} + p(0, 0, 1, 0, v)^t, && \vec{h}(\vec{q}) = w\vec{q} + p(0, 0, 0, 1, w)^t \end{aligned} \tag{2}$$

and

$$\begin{aligned} \vec{r}(\vec{q}) &= \mu(0, \tau_{11}, \tau_{21}, \tau_{31}, \sigma_1)^t, \\ \vec{s}(\vec{q}) &= \mu(0, \tau_{12}, \tau_{22}, \tau_{32}, \sigma_2)^t, \\ \vec{t}(\vec{q}) &= \mu(0, \tau_{13}, \tau_{23}, \tau_{33}, \sigma_3)^t, \end{aligned} \tag{3}$$

with the components of the viscous stress tensor given by

$$\begin{aligned} \tau_{11} &= \tfrac{4}{3}u_x - \tfrac{2}{3}v_y - \tfrac{2}{3}w_z, \\ \tau_{21} &= \tau_{12} = u_y + v_x, \\ \tau_{31} &= \tau_{13} = u_z + w_x, \\ \tau_{22} &= \tfrac{4}{3}v_y - \tfrac{2}{3}u_x - \tfrac{2}{3}w_z, \\ \tau_{32} &= \tau_{23} = v_z + w_y, \\ \tau_{33} &= \tfrac{4}{3}w_z - \tfrac{2}{3}u_x - \tfrac{2}{3}v_y, \end{aligned} \tag{4}$$

and

$$\begin{aligned} \sigma_1 &= u\tau_{11} + v\tau_{12} + w\tau_{13} + \frac{1}{(\gamma - 1)\mathrm{Pr}}(c^2)_x, \\ \sigma_2 &= u\tau_{21} + v\tau_{22} + w\tau_{23} + \frac{1}{(\gamma - 1)\mathrm{Pr}}(c^2)_y, \\ \sigma_3 &= u\tau_{31} + v\tau_{32} + w\tau_{33} + \frac{1}{(\gamma - 1)\mathrm{Pr}}(c^2)_z. \end{aligned} \tag{5}$$

Also, μ is the viscosity, γ is the ratio of specific heats, Pr is the Prandtl number, and

$$\begin{aligned} p &= (\gamma - 1)\left[E - \tfrac{1}{2}\rho(u^2 + v^2 + w^2)\right], \\ c^2 &= \frac{\gamma p}{\rho}, \\ H &= \frac{E + p}{\rho}. \end{aligned}$$

For implementing ENO schemes with characteristic decompositions, we need the expressions of the eigenvalues and the right and left eigenvectors of the Jacobians $\partial\vec{f}/\partial\vec{q}$, $\partial\vec{g}/\partial\vec{q}$, $\partial\vec{h}/\partial\vec{q}$. The eigenvalues for $\partial\vec{f}/\partial\vec{q}$ are $u-c$, u, u, u, $u+c$. Its right eigenvectors are the columns of

$$R=\begin{pmatrix} 1 & 0 & 0 & 1 & 1 \\ u-c & 0 & 0 & u & u+c \\ v & 1 & 0 & v & v \\ w & 0 & 1 & w & w \\ H-uc & v & w & \frac{1}{2}(u^2+v^2+w^2) & H+uc \end{pmatrix}, \tag{7}$$

and the left eigenvectors are the rows of

$$R^{-1}=\frac{1}{2}\begin{pmatrix} (b_2+u/c) & (b_1u+1/c) & -b_1v & -b_1w & b_1 \\ -2v & 0 & 2 & 0 & 0 \\ -2w & 0 & 0 & 2 & 0 \\ 2(1-b_2) & 2b_1u & 2b_1v & 2b_1w & -2b_1 \\ (b_2-u/c) & -(b_1u-1/c) & -b_1v & -b_1w & b_1 \end{pmatrix}, \tag{8}$$

with

$$b_1=\frac{\gamma-1}{c^2}, \qquad b_2=\tfrac{1}{2}(u^2+v^2+w^2)b_1. \tag{9}$$

The corresponding expressions for $\partial\vec{g}/\partial\vec{q}$ and $\partial\vec{h}/\partial\vec{q}$ are apparent.

The Euler equations can be obtained from the Navier–Stokes equations by setting $\mu=0$. The equations for two-dimensional problems are equally obvious.

In the two-dimensional case, the transformation

$$x=x(\xi,\eta), \qquad y=y(\xi,\eta), \tag{10}$$

enables us to treat non-uniform grids or mappings into nonrectangular domains. The Navier–Stokes equations become

$$\hat{q}_t+\hat{f}_\xi+\hat{g}_\eta=\hat{r}_\xi+\hat{s}_\eta, \tag{11}$$

where

$$\begin{aligned} \hat{q}&=J^{-1}\vec{q}, \\ \hat{f}&=J^{-1}\left[U\vec{q}+p(0,\xi_x,\xi_y,U)^{\mathrm{t}}\right], \\ \hat{g}&=J^{-1}\left[V\vec{q}+p(0,\eta_x,\eta_y,V)^{\mathrm{t}}\right], \\ \hat{r}&=J^{-1}\left(\xi_x\vec{r}+\xi_y\vec{s}\right), \\ \hat{s}&=J^{-1}\left(\eta_x\vec{r}+\eta_y\vec{s}\right), \\ \vec{r}&=\mu(0,\tau_{11},\tau_{21},\sigma_1)^{\mathrm{t}}, \\ \vec{s}&=\mu(0,\tau_{12},\tau_{22},\sigma_2)^{\mathrm{t}}, \end{aligned} \tag{12}$$

with

$$\begin{aligned}
\tau_{11} &= \tfrac{4}{3}(\xi_x u_\xi + \eta_x u_\eta) - \tfrac{2}{3}(\xi_y v_\xi + \eta_y v_\eta),\\
\tau_{21} &= \tau_{12} = \xi_y u_\xi + \eta_y u_\eta + \xi_x v_\xi + \eta_x v_\eta,\\
\tau_{22} &= \tfrac{4}{3}(\xi_y v_\xi + \eta_y v_\eta) - \tfrac{2}{3}(\xi_x u_\xi + \eta_x u_\eta),\\
\sigma_1 &= u\tau_{11} + v\tau_{12} + \frac{1}{(\gamma-1)\mathrm{Pr}}\left[\xi_x (c^2)_\xi + \eta_x (c^2)_\eta\right],\\
\sigma_2 &= u\tau_{21} + v\tau_{22} + \frac{1}{(\gamma-1)\mathrm{Pr}}\left[\xi_y (c^2)_\xi + \eta_y (c^2)_\eta\right],
\end{aligned} \tag{13}$$

and

$$\begin{aligned}
J &= \xi_x \eta_y - \xi_y \eta_x,\\
U &= \xi_x u + \xi_y v,\\
V &= \eta_x u + \eta_y v.
\end{aligned} \tag{14}$$

The eigenvalues for $\partial \hat{f}/\partial \hat{q}$ are $U - c\sqrt{\xi_x^2 + \xi_y^2}$, U, U, $U + c\sqrt{\xi_x^2 + \xi_y^2}$; the right eigenvectors are the columns of

$$R = \begin{pmatrix} 1 & c & 1 & 1 \\ u - \tilde{\xi}_x c & -\tilde{\xi}_y & u & u + \tilde{\xi}_x c \\ v - \tilde{\xi}_y c & \tilde{\xi}_x & v & v + \tilde{\xi}_y c \\ H - \theta_\xi c & -\tilde{\xi}_y u + \tilde{\xi}_x v & \tfrac{1}{2}(u^2 + v^2) & H + \theta_\xi c \end{pmatrix}; \tag{15}$$

the left eigenvectors are the rows of

$$R^{-1} = \frac{1}{2}\begin{pmatrix} \left(b_2 + \tilde{\theta}_\xi/c\right) & -\left(b_1 u + \tilde{\xi}_x/c\right) & -\left(b_1 v + \tilde{\xi}_y/c\right) & b_1 \\ 2\left(\tilde{\xi}_y u - \tilde{\xi}_x v\right) & -2\tilde{\xi}_y & 2\tilde{\xi}_x & 0 \\ 2(1 - b_2) & 2b_1 u & 2b_1 v & -2b_1 \\ \left(b_2 - \tilde{\theta}_\xi/c\right) & -\left(b_1 u - \tilde{\xi}_x/c\right) & -\left(b_1 v - \tilde{\xi}_y/c\right) & b_1 \end{pmatrix}, \tag{16}$$

where b_1 and b_2 are defined in (2.8); and

$$\begin{aligned}
\tilde{\xi}_x &= \frac{\xi_x}{\sqrt{\xi_x^2 + \xi_y^2}}, \qquad \tilde{\xi}_y = \frac{\xi_y}{\sqrt{\xi_x^2 + \xi_y^2}},\\
\tilde{\theta}_\xi &= \tilde{\xi}_x u + \tilde{\xi}_y v.
\end{aligned} \tag{17}$$

We again forego the explicit prescription for $\partial \hat{g}/\partial \hat{q}$.

3. Implementing the ENO schemes

This section should be read in conjunction with [22,23] for notation, terminology and other details of ENO schemes based on fluxes and for TVD time-discretizations of Runge–Kutta type. Here we only summarize several key steps of the algorithms and address practical issues such as vectorization, efficiency, cost comparison and the reduction of round-off errors.

The ENO procedure is applied only to the convection part, i.e., the left-hand side, of (1). The diffusion right-hand side of (1) is approximated by the standard centered differences. It is also possible to use ENO-type adaptive stencil interpolation to approximate the diffusion terms, but we have not observed any significant differences in our numerical tests (typically with small physical viscosity ν). Besides simplicity, centered approximations also seem more natural for diffusion terms.

We now summarize the key steps of the algorithm:

(1) The time marching is implemented by a class of TVD Runge–Kutta type methods [22]. For example, the third-order case is

$$\begin{aligned}
\vec{q}^{(1)} &= \vec{q}^{(0)} + \Delta t \vec{L}(\vec{q}^{(0)}),\\
\vec{q}^{(2)} &= \tfrac{3}{4}\vec{q}^{(0)} + \tfrac{1}{4}\vec{q}^{(1)} + \tfrac{1}{4}\Delta t \vec{L}(\vec{q}^{(1)}),\\
\vec{q}^{(3)} &= \tfrac{1}{3}\vec{q}^{(0)} + \tfrac{2}{3}\vec{q}^{(2)} + \tfrac{2}{3}\Delta t \vec{L}(\vec{q}^{(2)}),\\
\vec{q}^{(0)} &= \vec{q}^{n}, \qquad \vec{q}^{n+1} = \vec{q}^{(3)},
\end{aligned} \tag{18}$$

where $\vec{L}$ is the numerical spatial operator approximating the spatial derivatives in (2). This class of Runge–Kutta methods is labeled TVD because it has been shown [22] that it does not increase the total variation of the spatial part under a suitable CFL restriction. Also notice that for the third-order case (18) only three storage levels (two for $\vec{q}$, one for $\vec{L}$) are needed, since $\vec{q}^{(2)}$ can overwrite $\vec{q}^{(1)}$ and $\vec{q}^{(3)}$ can again overwrite $\vec{q}^{(1)}$.

(2) We thus only need to consider the spatial operator

$$\vec{L}(\vec{q}) = -\vec{f}(\vec{q})_x - \vec{g}(\vec{q})_y - \vec{h}(\vec{q})_z + \vec{r}(\vec{q})_x + \vec{s}(\vec{q})_y + \vec{t}(\vec{q})_z. \tag{19}$$

The last three terms are approximated by standard second-order or fourth-order centered differences. We use an ENO scheme based on fluxes; hence the first three terms can be approximated dimension-by-dimension: for example, when approximating $-\vec{f}(\vec{q})_x$, y and z are fixed. The core of the algorithm is then a one-dimensional ENO approximation to, e.g., $-\vec{f}(\vec{q})_x$.

(3) Since $\vec{f}(\vec{q})$ is a vector, we can approximate $-\vec{f}(\vec{q})_x$ either component by component, or in (local) characteristic directions. In the former case, to obtain nonlinear stability by upwinding, we write

$$\vec{f}(\vec{q}) = \vec{f}^{+}(\vec{q}) + \vec{f}^{-}(\vec{q}), \tag{20}$$

with

$$\vec{f}^{\pm}(\vec{q}) = \tfrac{1}{2}\left(\vec{f}(\vec{q}) \pm \alpha \vec{q}\right), \tag{21}$$

where $\alpha = \max(|u| + c)$ is the largest eigenvalue in absolute value of the Jacobian $\partial \vec{f}/\partial \vec{q}$ along the relevant x-line. The decomposition in (20) guarantees that $\partial \vec{f}^{\pm}/\partial \vec{q}$ has positive/negative

eigenvalues; hence upwinding (to be discussed later in this section) is the same for all components. For characteristic decompositions, we take $A_{j+1/2}$ to be some average Jacobian at $x_{j+1/2}$, e.g., the arithmetic mean

$$A_{j+1/2} = \left.\frac{\partial \vec{f}}{\partial \vec{q}}\right|_{\vec{q}=(\vec{q}_j+\vec{q}_{j+1})/2} \tag{22}$$

or

$$A_{j+1/2} = \left.\frac{\partial \vec{f}}{\partial \vec{q}}\right|_{\vec{q}=\vec{q}^{\,\mathrm{Roe}}_{j+1/2}}, \tag{23}$$

where $\vec{q}^{\,(\mathrm{Roe})}_{j+1/2}$ is the Roe average of $\vec{q}_j$ and $\vec{q}_{j+1}$ [17]. We then use the left eigenvectors $R^{-1}_{j+1/2}$ in (8) or (16) of $A_{j+1/2}$ to project all relevant quantities (differences around $x_{j+1/2}$) to the local characteristic fields. A scalar ENO algorithm can then be applied, and the result projected back to component space by $R_{j+1/2}$ in (7) or (15).

(4) We finally describe the implementation of the scalar ENO approximation of $-f(q)_x$. It is written as a conserved flux difference

$$-f(q)_x|_{x=x_j} \approx -\frac{1}{\Delta x}\left(\hat{f}_{j+1/2}-\hat{f}_{j-1/2}\right), \tag{24}$$

where the numerical flux $\hat{f}_{j+1/2}$ approximates $h(x_{j+1/2})$ to a high order with $h(x)$ defined by

$$f(u(x)) = \frac{1}{\Delta x}\int_{x-(\Delta x)/2}^{x+(\Delta x)/2} h(\xi)\,\mathrm{d}\xi. \tag{25}$$

It is pointed out in [23] that we do not need to construct $h(x)$ explicitly: we simply use the difference tables of $f(u(x))$. If the (undivided) differences of $f(u(x))$ are defined by

$$\begin{aligned} &f[j, 0] = f(u_j), \\ &f[j, k] = f[j+1, k-1] - f[j, k-1], \quad k = 1, \ldots, r, \end{aligned} \tag{26}$$

where r is the spatial order, then

$$\hat{f}_{j+1/2} = \sum_{m=0}^{r} c(i-j, m) f[i, m], \tag{27}$$

with i being the left-most point in the stencil used to approximate $\hat{f}_{j+1/2}$, and $c(s, m)$ being defined by

$$c(s, m) = \frac{1}{(m+1)!}\sum_{l=s}^{s+m}\prod_{\substack{p=s \\ p\neq l}}^{s+m}(-p). \tag{28}$$

The small, constant matrix c is computed once and stored.

The adaptive stencil is determined by the choice of i, the left-most point in the stencil used to approximate $\hat{f}_{j+1/2}$. We start with $i=j$ or $i=j+1$ according to the (local) wind direction (upwinding), and then apply the following

```
if (abs(f[i,k]).gt.abs(f[i-1,k])) i=i-1
```
(29)

for $k = 1, \ldots, r$.

Remark 3.1. The code is written in such a way that all the major loops are vectorized by default of Cray Fortran. To vectorize (27)–(29) we can either repeat (29) r times (for fixed r only) or introduce a temporary one-dimensional storage for i to put the short loop (29) outside the long loop (27)–(29) for j. To vectorize the characteristic decompositions we have to introduce one-dimensional temporary storage for the local projection on characteristic fields at each x_j. Since we only vectorize the innermost one-dimensional loop, we need just 17 three-dimensional units (10 for two components of $\vec{q}$, 5 for $\vec{L}$, and 2 work units) for three-dimensional problems using third-order schemes.

Remark 3.2. For our current implementation, the componentwise ENO scheme takes around 4.5 times as much CPU time as a centered finite-difference scheme with the same order of accuracy. A factor of two is due to the flux splitting (29). Instead of just computing $\vec{f}(\vec{q})_x$ we are computing $\vec{f}^+(\vec{q})_x + \vec{f}^-(\vec{q})_x$; hence the work is doubled. This is the price to pay for implementing upwinding techniques to achieve stability. Another factor of two is due to the adaptive stencil procedure (20): when these "if" statements are removed, the code runs twice as fast. It seems odd that these "if" statements account for so much CPU time since they are all vectorized. The main reason is that since the pattern is not uniform from point to point, gathering and scattering are activated by Cray Fortran. These procedures are very slow on the Cray. A similar slow-down also exists for TVD schemes. ENO schemes using characteristic decompositions take more CPU time: ENO-LF and ENO-Roe with entropy fix (see [23] for definitions) take about 3 and 1.7 times, respectively, as much CPU time as componentwise ENO schemes. Notice that ENO-Roe is faster than ENO-LF because it does not use a flux splitting. See [23] for more details.

Remark 3.3. We use undivided differences (26), and prestored local matrix c (28), to reduce cost and to reduce the effect of round-off errors.

4. Transition in a free shear layer

The numerical examples were chosen to illustrate the ENO method for problems in transition and turbulence. We consider flows with gradients which are readily resolved by the grid—shocks are either absent altogether or else sufficiently broad (due to low Reynolds number) that the usual spectral method gives stable results. Comparisons of the intrinsic resolution can therefore be made between the spectral and ENO methods. We then take strong shock cases to illustrate the advantage of non-oscillatory high-order methods.

Unless otherwise indicated, third-order ENO with the third-order Runge–Kutta time discretization (18) and fourth-order centered differences for the viscous terms are used. Notice that the third-order ENO [23] is actually fourth-order in smooth, monotone regions; hence for problems with isolated critical points it is fourth-order in L_1 norm sense. We use, as in [23], the notations ENO-LF (Lax–Friedrichs), ENO-Roe and ENO-Com (componentwise).

There has been considerable recent interest in the physics of the compressible free shear layer and numerical simulations have furnished several interesting results. The numerical methods employed have typically been second-order TVD [24,12], fourth-order MacCormack

[25, 16], or fourth- or even sixth-order compact [10, 19, 2]. Atkins [1] and Sandham and Yee [20] have made detailed studies of the performance of TVD schemes on this problem. The latter also made comparisons with second-order MacCormack results. Carpenter, et al. [2] have compared third-order upwind, fourth-order MacCormack and fourth-order compact methods.

For the particular 2D examples studied in the present paper, the mean flow is given by the hyperbolic tangent profile $u_0 = \tanh(y)$, $v_0 = 0$, and $p_0 = 1/(\gamma M_\infty^2)$, where M_∞ is the ratio in the limit $y \to \pm\infty$, of the freestream velocity to the sound speed, and periodic boundary conditions are enforced in the streamwise (x) direction. The velocity is nondimensionalized by the freestream velocity u_∞, lengths by half the vorticity thickness $\delta_w = 2u_0/|\partial u_0/\partial y|$, the density by the freestream density ρ_∞, the temperature by the freestream temperature T_∞, and the pressure by $\rho_\infty u_\infty^2$. The Reynolds number $\mathrm{Re} = u_0 \delta_w \rho_\infty / \mu_\infty$. The viscosity μ is prescribed through Sutherland's law with a reference temperature of 520 °K and the Prandtl number is taken to be 0.7. This example is for the temporally evolving free shear layer. A forcing term is added to the Navier–Stokes equations in order to make the assumed mean flow a steady solution. The computational domain is $(0, 2\pi/\alpha) \times (-\infty, \infty)$, where α is a specified wavelength.

For this problem we present comparisons of ENO with both explicit and compact centered difference schemes and with spectral methods. The explicit central difference methods use 3 points for a second-order approximation and 5 points for fourth-order. The compact difference scheme uses a Padé approximation with 5 explicit points and 3 implicit points (see [10]). It is formally sixth-order accurate at all interior points, and at points adjacent to the boundary, but reduces to fourth-order accuracy at the boundary itself. (The sixth-order compact scheme used by Lele [10] reduces to fourth-order accuracy at points adjacent to the boundary and third-order accuracy at the boundary itself.) For the spectral calculation a Fourier expansion is applied in x and the Cain transformation [3]

$$y = -L \cot(\eta) \tag{30}$$

is used in the y direction; L is a stretching parameter which is taken between 4 and 10. This permits the use of cosine (for ρ, u, and E) and sine (for v) expansions of the dependent variables in the η direction.

4.1. Linear instability

For the smooth problem we consider first the evolution of a small perturbation, with streamwise wavenumber $\alpha = 0.4$, from the mean flow at $M_\infty = 0.5$ with a Reynolds number of 100, and the usual $\gamma = 1.4$. The shape of the perturbation is given by the fastest growing eigenfunction of the linearized Navier–Stokes equations at the specified wavelength. The amplitude of the perturbation was chosen so that its transverse velocity at $y = 0$ was 0.1% of the freestream velocity. The growth rate for this particular case was 0.127454941. (This eigenvalue problem was solved by a spectral linear stability code [11].) For such small amplitudes the nonlinear code should produce linear growth of the perturbations for small times. Table 1 shows the growth rates produced by central difference methods and compact methods after 10 time-steps with a time-step of 0.01. (The measured growth rate was taken to be $\sigma = [\log E(t) - \log E(0)]/(2t)$ where $E(t) = \| u - u_0 \|_{L^2}^2 + \| v \|_{L^2}^2$.) In these examples a highly resolved discretization (with 128 points) was employed in y and the specified method was applied in x with the streamwise resolution as noted in the table. The table thus provides

Table 1
Linear growth rate errors for central-difference and compact schemes at $t = 0.1$

Method	$N_x = 8$	$N_x = 16$	$N_x = 32$
2nd-order central	−4.26 (−2)	−6.26 (−3)	−1.24 (−3)
4th-order central	−4.92 (−3)	−1.83 (−4)	−1.35 (−5)
4th-order compact	2.15 (−4)	1.25 (−5)	5.00 (−7)
6th-order compact	1.12 (−5)	1.90 (−8)	−2 (−8)

the accuracy achieved as a function of the method and the number of grid-points per wavelength. (Even for $N_x = 4$, the error from a spectral discretization in x is already smaller than 10^{-7}.)

Similar results for ENO methods of second-, third- and fourth-order are given in Table 2. In these cases the ENO method was also applied in y, again with 128 points used in this direction. Again, the intent was to isolate the discretization errors in x. Except for the $N_x = 64$ cases, the results are as one would expect: the accuracy increases with the number of grid-points and with the order of the scheme. (The unexpected deterioration of the convergence rate for the finest grid is addressed below.) A comparison of the fourth-order central-difference results from Table 1 with those of the third-order ENO from Table 2 indicates that the ENO results are slightly less accurate. This is to be expected since one anticipates that in most of the flow this ENO stencil reduces to the fourth-order central one, and where it is switched to one-sided it will lose one order in accuracy.

Notice that the improvement in accuracy obtained from going from 32 to 64 streamwise grid-points is less than expected. For the central-difference schemes this occurs on the 10^{-6} level, whereas it occurs an order of magnitude or more earlier for the ENO schemes. (This is even more apparent in the ENO results at later times, as evidenced by the data in Table 3.) This is due to time-differencing and linearization errors for the central-difference methods, whereas it is caused by the loss of accuracy when the stencil switches for the ENO method. The results labelled by "ENO-2" in the tables are computed by using a factor of 2 to multiply either the first or the second abs term in (29), depending upon whether i is greater than the left-most point in the centered stencil or not. The effect is to bias the scheme towards a centered stencil in smooth regions. This modification of ENO is discussed in detail in [21], accompanied by numerical tests on smooth and shocked cases, in response to a recent discovery by Rogerson

Table 2
Linear growth rate errors for ENO schemes at $t = 0.1$

Method	$N_x = 8$	$N_x = 16$	$N_x = 32$	$N_x = 64$
2nd-order ENO	−4.30 (−2)	−6.30 (−3)	−1.14 (−3)	−4.90 (−4)
2nd-order ENO-2	−3.83 (−2)	−2.01 (−3)	−8.28 (−4)	−5.58 (−4)
3rd-order ENO	−1.62 (−2)	−1.05 (−3)	−1.48 (−4)	−9.85 (−5)
3rd-order ENO-2	−8.77 (−3)	−3.38 (−5)	−2.20 (−6)	−2.51 (−6)
4th-order ENO	−4.96 (−3)	−1.88 (−4)	−1.54 (−5)	−9.88 (−6)
4th-order ENO-2	−4.21 (−3)	−1.28 (−5)	−1.39 (−5)	−1.78 (−5)

Table 3
Linear growth rate errors at $t = 1.0$

Method	$N_x = 8$	$N_x = 16$	$N_x = 32$	$N_x = 64$
2nd order ENO	−4.26 (−2)	−6.37 (−3)	−1.26 (−3)	−6.20 (−4)
2nd order ENO-2	−3.86 (−2)	−1.43 (−3)	−8.33 (−4)	−5.72 (−4)
3rd-order centered	−4.22 (−2)	−6.21 (−3)	−1.23 (−3)	−5.89 (−4)
3rd-order ENO	−1.59 (−2)	−1.16 (−3)	−2.41 (−4)	−1.89 (−4)
3rd-order ENO-2	−7.31 (−3)	1.55 (−5)	−2.52 (−5)	−3.49 (−5)
4th-order centered	1.04 (−3)	3.55 (−5)	−3.14 (−5)	−3.56 (−5)
4th-order ENO	−4.95 (−3)	−2.53 (−4)	−9.35 (−5)	−7.79 (−5)
4th-order ENO-2	−4.19 (−3)	−5.03 (−5)	−3.12 (−5)	−2.92 (−5)
5th-order centered	−4.92 (−3)	−2.14 (−4)	−4.63 (−5)	−4.09 (−5)

and Meiberg [18] about some accuracy degeneracy phenomena of ENO schemes. From the table we can see that "ENO-2" is in most cases comparable in accuracy with the corresponding centered schemes, while ENO is usually one order lower, as expected from the (unnecessary) switching of stencils in smooth regions.

4.2. Mach 0.5 evolution

Next, we present a comparison of these methods for a fully nonlinear problem. The previous results were just basic calibration tests (for all the methods). The real purpose of numerical simulation codes is to explore nonlinear fluid dynamics. The next example, therefore, is a simulation of vortex roll-up and pairing at $M_\infty = 0.5$. The initial conditions consist of the mean flow plus two linear eigenfunctions: the fundamental with wavenumber $\alpha_f = 0.4$ and amplitude $\epsilon_f = 0.01$ and its subharmonic with wavenumber $\alpha_s = 0.2$ and amplitude $\epsilon_s = 0.0001$. (In this case the computational domain in x is doubled from that of the previous example in order to accommodate the subharmonic.) The initial phases (judged by the location of the maximum of the normal velocity perturbation at $y = 0$) were exactly out of phase, a choice which ensures that vortex pairing will occur.

Figure 1 presents the evolution of the vorticity thickness for third-order ENO on grids of size 32^2, 64^2, and 128^2 and compares these results with those of a 128^2 spectral calculation. (An analysis of the spectral coefficients of the latter coefficients, along the lines discussed in [26], indicates that the spectral result is accurate to better than 4 significant digits until about $t = 125$, but that thereafter its accuracy deteriorates rapidly as the vortex roll-up produces scales, particularly in the streamwise direction, that are too small for the grid.) The ENO result is clearly converging to the proper answer. A similar comparison is presented for the sixth-order compact scheme in Fig. 2. The convergence here is more impressive than for the ENO scheme, but that is to be expected for this smooth flow. Curiously, the spectral coefficients for the compact scheme suggest that it is the transverse resolution which is most stressed by the roll-up.

Figure 3 summarizes, for the third-order ENO method, the evolution of the lowest 4 Fourier harmonics as represented by the quantity

$$E_k = \int_{-\infty}^{\infty} \left(|\hat{u}_k|^2 + |\hat{v}_k|^2 \right) W(y)\, \mathrm{d}y \tag{31}$$

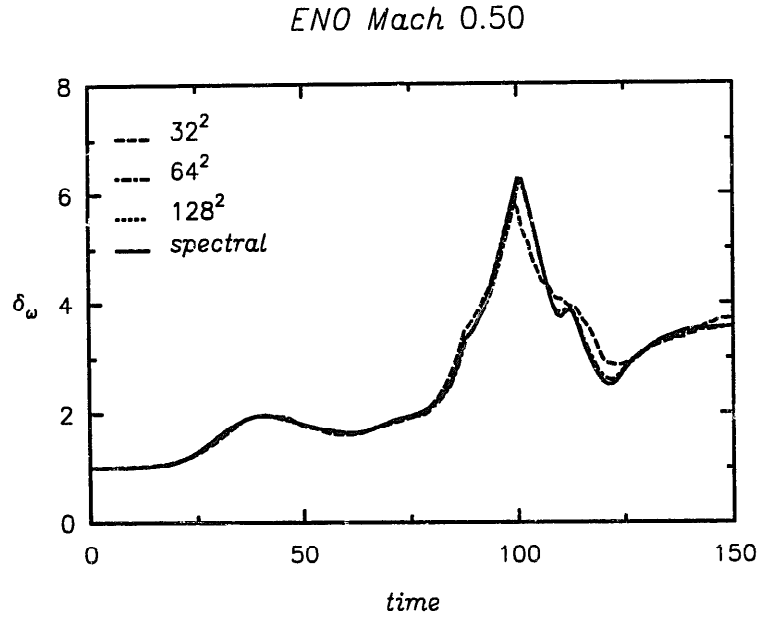

Fig. 1. Evolution of the vorticity thickness for the Mach 0.5 free shear layer problem using the third-order ENO scheme.

where

$$\hat{q}_k(y, t) = \frac{\alpha_s}{2\pi} \int_0^{2\pi/\alpha_s} q(x, y, t)\, e^{-ik\alpha_s x}\, dx \tag{32}$$

is the kth streamwise Fourier coefficient of the variable q and

$$W(y) = \begin{cases} 1, & |y| \leqslant y_c, \\ e^{-(|y|-y_c)^2}, & |y| > y_c \end{cases} \tag{33}$$

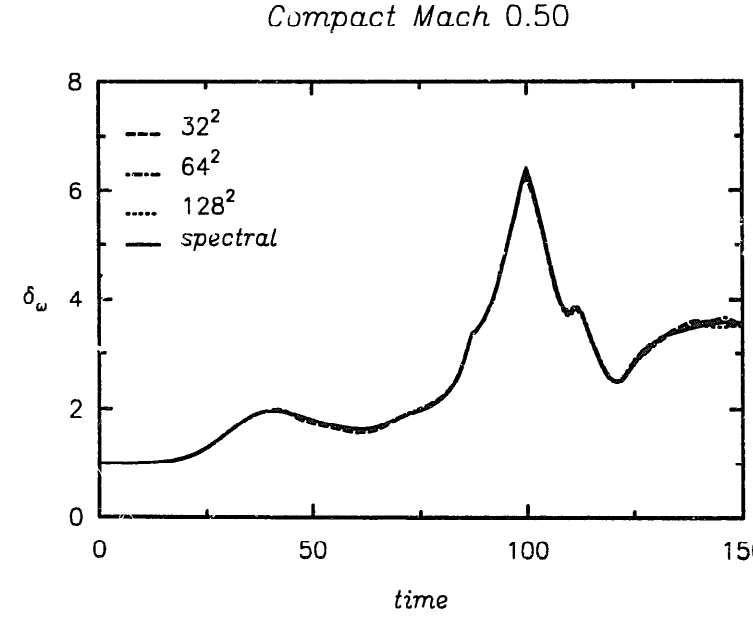

Fig. 2. Evolution of the vorticity thickness for the Mach 0.5 free shear layer problem using the sixth-order compact scheme.

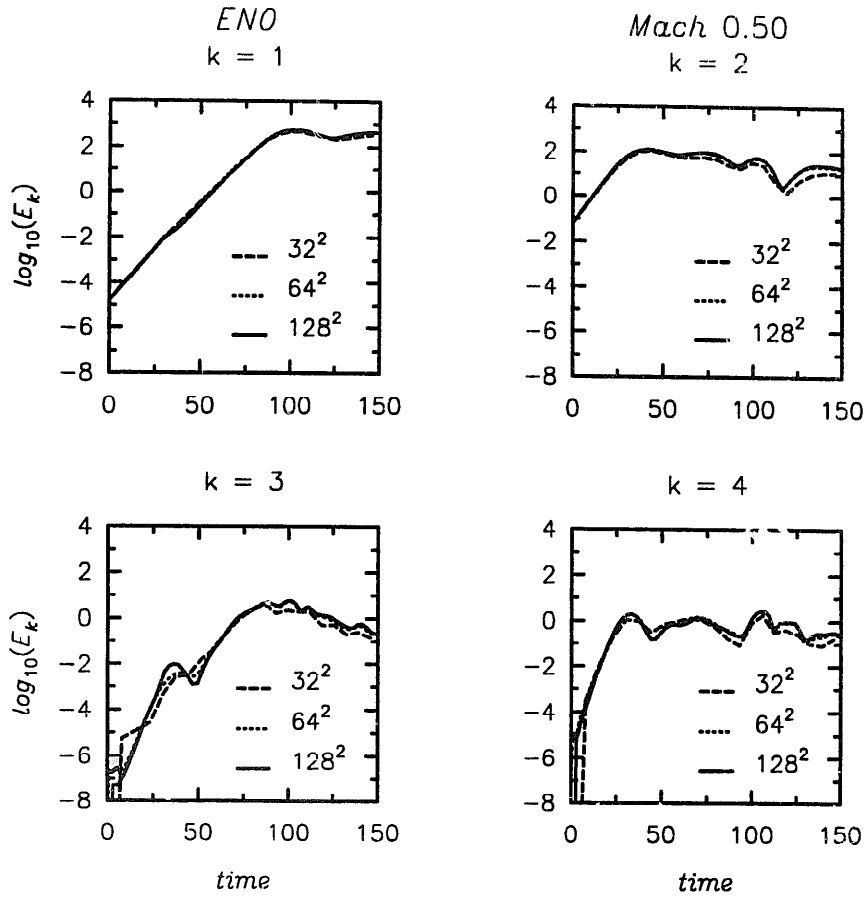

Fig. 3. Evolution of the 4 lowest Fourier harmonics for the Mach 0.5 free shear layer problem using the third-order ENO scheme.

is a weight function used to confine the region of integration to a finite size. (We used $y_c = 50$.) Once again, the numerical results are indicative of convergence. On a 32^2 grid the ENO results are perceptibly different from the highly resolved results even for the $k = 1$ mode. On a 64^2 grid the worst relative results occur for $k = 3$. This mode happens to be the most sensitive of the 4 to nonlinear interactions. At the start of the calculation only the $k = 1$ and $k = 2$ modes have nonzero amplitudes. The $k = 2$ mode is initially forced by the self-interaction of the $k = 2$ mode, which is the dominant mode for the first part of the calculation. The $k = 3$ mode is initially forced by the interaction between the $k = 1$ and $k = 2$ modes and it is here that the largest errors occur. One heartening result is that the $k = 1$ mode—the subharmonic—is tracked reasonably well. Atkins [1] observed that there could be appreciable spurious generation of this mode by a second-order TVD method.

Similar data are provided in Fig. 4 for the compact scheme. The results for these low-order modes are already graphically indistinguishable from the 128^2 spectral results on a 64^2 grid for the compact scheme. This, too, is understandable since the compact scheme was shown in Table 1 to have an accuracy of better than 1 part in 10^4 with 8 points per wavelength, and even the mode $k = 4$ has 8 points per wave.

We close the Mach 0.5 results with a plot, in Fig. 5, of the pressure contours at $t = 150$ for the ENO method on various grids and for the high-resolution spectral method. The similarity of all the results is apparent.

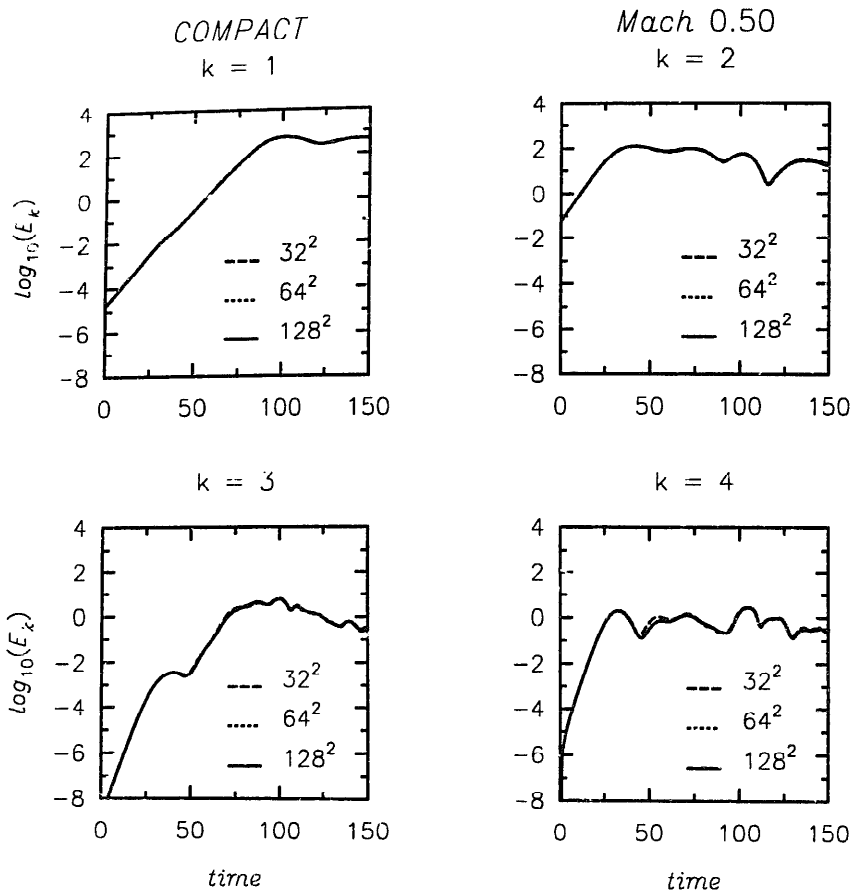

Fig. 4. Evolution of the 4 lowest Fourier harmonics for the Mach 0.5 free shear layer problem using the sixth-order compact scheme.

4.3. Mach 0.9 evolution

The rationale for the ENO method rests primarily on its behavior in the presence of shocks. Indeed, typical central-difference and spectral methods have substantial difficulty for this compressible free layer problem at freestream Mach numbers above 0.70. For this example we choose $M_\infty = 0.9$ and initial conditions consisting of the mean flow plus two linear eigenfunctions: the fundamental with wavenumber $\alpha_f = 0.3$ and amplitude $\epsilon_f = 0.01$ and its subharmonic with wavenumber $\alpha_s = 0.15$ and amplitude $\epsilon_s = 0.001$. Furthermore, the stretching parameter

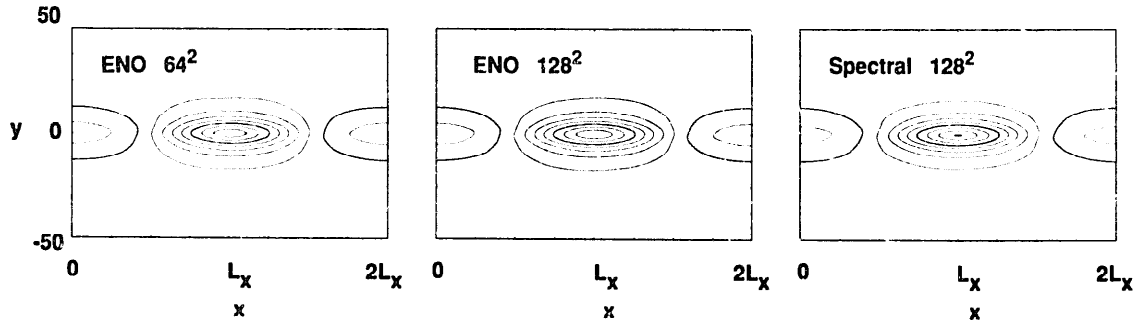

Fig. 5. Pressure field at $t = 150$ for the Mach 0.5 free shear layer problem.

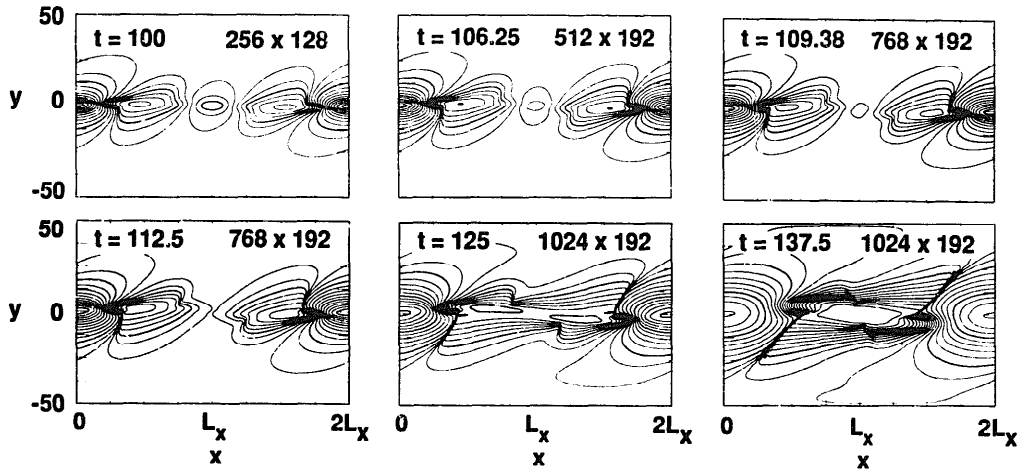

Fig. 6. Pressure field for the Mach 0.9 free shear layer problem using the sixth-order compact scheme.

for the ENO method is here chosen to be $L = 10$ to provide better resolution near the shock waves which eventually develop.

The evolution of the pressure field for this case is depicted in Fig. 6. These plots are taken from a computation based on the sixth-order compact scheme. (A 128^2 grid was used from $t = 0$ to $t = 75$, a 256×128 grid from $t = 75$ to $t = 100$, a 512×192 grid from $t = 100$ to $t = 106.25$, a 768×192 grid from $t = 106.25$ to $t = 112.5$, and a 1024×192 grid from $t = 112.5$ to $t = 137.5$. Spectral interpolation was employed for the requisite grid refinements.) By $t = 100$ vortex pairing has already occurred. The vortex is centered in the plotting frame and stagnation points are located on the vertical mid-plane at the streamwise edges of the plot. As discussed, for example, by Lele [10], the flow expands away from the stagnation points as it goes around the vortex and compresses as it returns to the stagnation point. At sufficiently high Mach numbers and for sufficiently strong vortices the compression occurs via a shock wave. Shortly after $t = 100$ in this case a pair of shocks develop—these are the so-called "eddy shicklets" [24, 10]—and they grow steadily stronger as the flow evolves. These shocks are not the only small-scale feature of the flow, however. As noted by Sandham and Yee [20], the flow also develops a very thin region of high strain near the stagnation points.

Although there is a physical viscosity in the flow (in this case the Reynolds number Re = 100), the thicknesses of the shock and/or high strain regions may eventually become too small for a central-difference scheme to handle. Such is the case here even on a 1024×192 mesh. In the presence of unresolved gradients central-difference schemes develop oscillations which lead to negative temperatures and an abrupt halt to the calculation.

Indeed, computations with both the spectral and the sixth-order schemes on 32^2, 64^2 and 128^2 grids develop severe oscillations and come to a crashing halt between $t = 105$ and $t = 110$. Somewhat curiously, as noted by Sandham (1990, private communication), for both methods the oscillations develop first not in the vicinity of the shock but in the region of high strain. This is particularly apparent in Fig. 7, which shows the evolution of the pressure for the spectral method calculation (in which a 128^2 grid was used from $t = 0$ to $t = 75$, a 256×128 grid from $t = 75$ to $t = 100$, a 384×128 grid from $t = 100$ to $t = 106.25$, a 768×144 grid from $t = 106.25$ to $t = 109.375$, and a 1024×162 grid from $t = 109.375$ to $t = 112.0$). The computation halted shortly after $t = 112$ due to negative temperatures caused by severe oscillations. Figure 8 is a

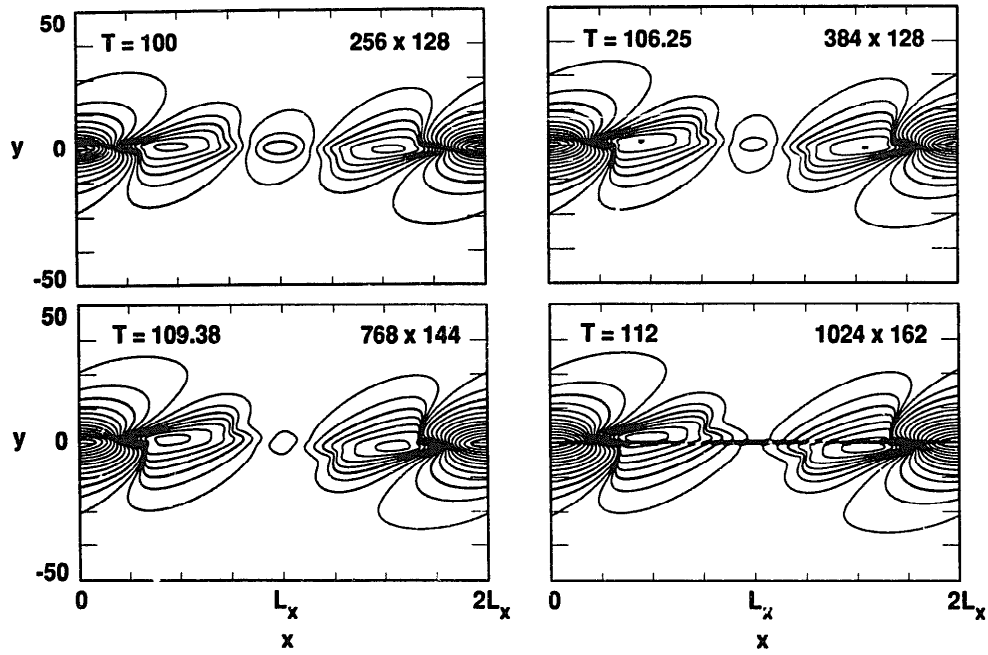

Fig. 7. Pressure field for the Mach 0.9 free shear layer problem using the spectral scheme.

blow-up of the central region at $t = 112$. Note that there are no oscillations apparent in the vicinity of the shocks. Note also that the oscillations are predominantly in the x direction. Indeed, an examination of the spectral coefficients reveals that the y direction is quite well-resolved. The price of resolving these regions with a nondissipative central-difference scheme can easily be excessive, as the present case indicates.

The vorticity thickness of the ENO and sixth-order compact methods are provided in Figs. 9 and 10, respectively. The results for ENO method demonstrate convergence—the vorticity thickness on the 128^2 grid is virtually coincident with the compact method result. The errors for the ENO method for this Mach 0.9 case are substantially larger than for the Mach 0.5 case (see Fig. 1). However, this is due primarily to the difference in the stretching parameter. For the

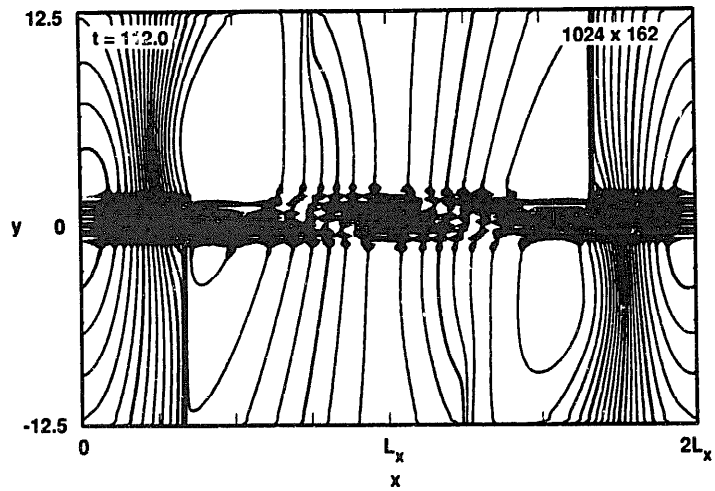

Fig. 8. Blow-up of the central region from the spectral results for the free shear layer problem at $t = 112$.

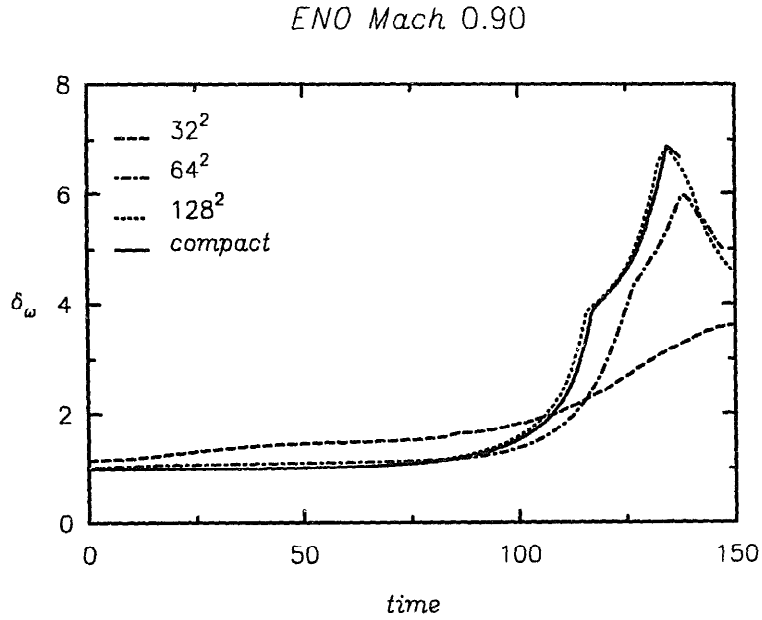

Fig. 9. Evolution of the vorticity thickness for the Mach 0.9 free shear layer problem using the third-order ENO scheme.

Mach 0.9 ENO calculations, a weaker transverse stretching was used to afford finer resolution in the vicinity of the shock.

Results for the lowest 4 Fourier harmonics for the two methods are given in Figs. 11 and 12. The performance of the two methods for this diagnostic mimic that for the vorticity thickness.

All of the results reported thus far have been for the ENO method using the characteristic decomposition. As noted at the end of Section 3, componentwise ENO is simpler to program

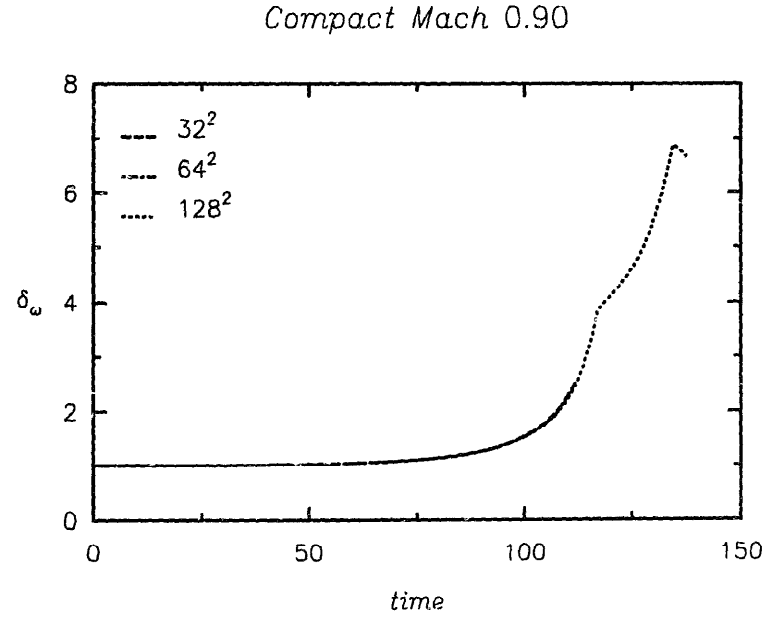

Fig. 10. Evolution of the vorticity thickness for the Mach 0.9 free shear layer problem using the sixth-order compact scheme.

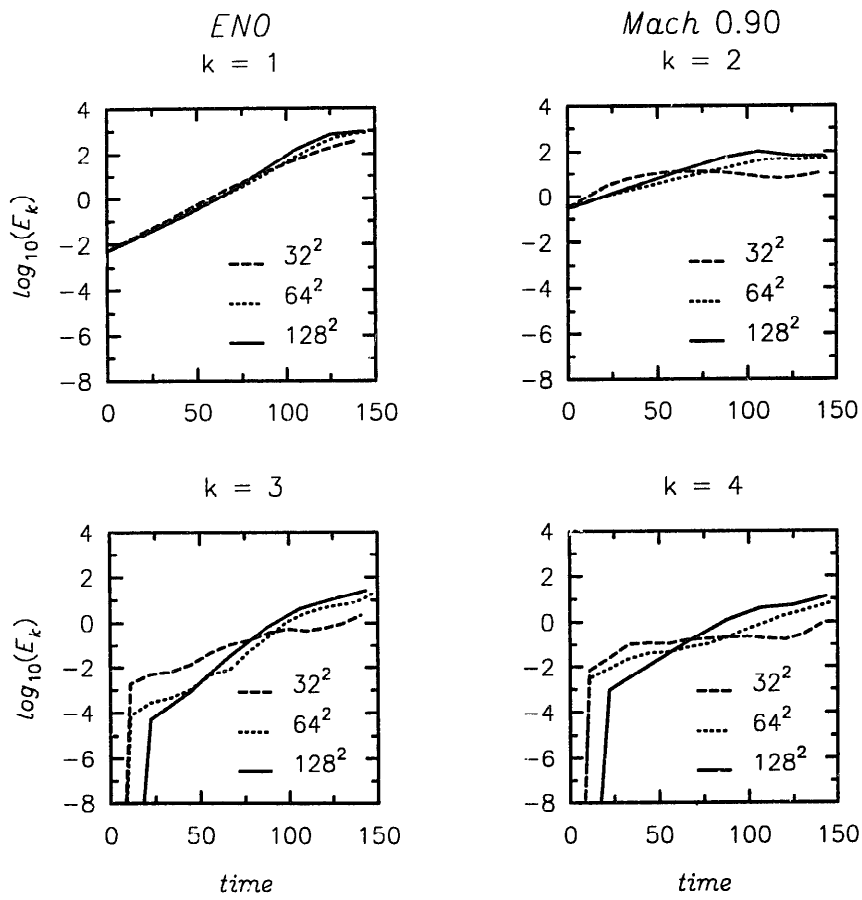

Fig. 11. Evolution of the 4 lowest Fourier harmonics for the Mach 0.9 free shear layer problem using the third-order ENO scheme.

and is less expensive. Figures 13 and 14 compare the two versions at $t = 125$ and $t = 150$, respectively. The componentwise results suffer in two respects. First, the shock is more diffuse. In fact, at $t = 125$ the shock is barely visible. Second, there are appreciable spurious oscillations. Their character is quite different from the oscillations which afflict the compact and spectral results. They are far less regular but are held in check by the nonlinearly stable adaptive stencil. Nevertheless, the small-scale flow features of the componentwise ENO results are quite unreliable. One must hesitate to use this method for applications in which the small scale features are of particular interest, such as transition to turbulence problems.

A comparison of the characteristicwise ENO results at $t = 125$ with those of the compact scheme (Fig. 6) reveals that even on a 128^2 grid the ENO method produces a numerical shock thickness which is much larger than the actual thickness for this viscous problem. Moreover, the absence of a shock on the 64^2 grid appears due to the delayed flow evolution (presumably caused by the inherent viscosity of the ENO method) that is apparent in Fig. 9.

We conclude the results for this problem with Fig. 15, which shows the long time evolution of a 64^2 characteristicwise ENO calculation based on the Euler equations (but starting with the same initial conditions as the Navier–Stokes calculation above). Even on this coarse grid, and without the aid of any physical viscosity, the ENO method exhibits solid shock-capturing behavior. The numerical solution shows no sign of nonlinear instability and spurious small-scale oscillations are absent.

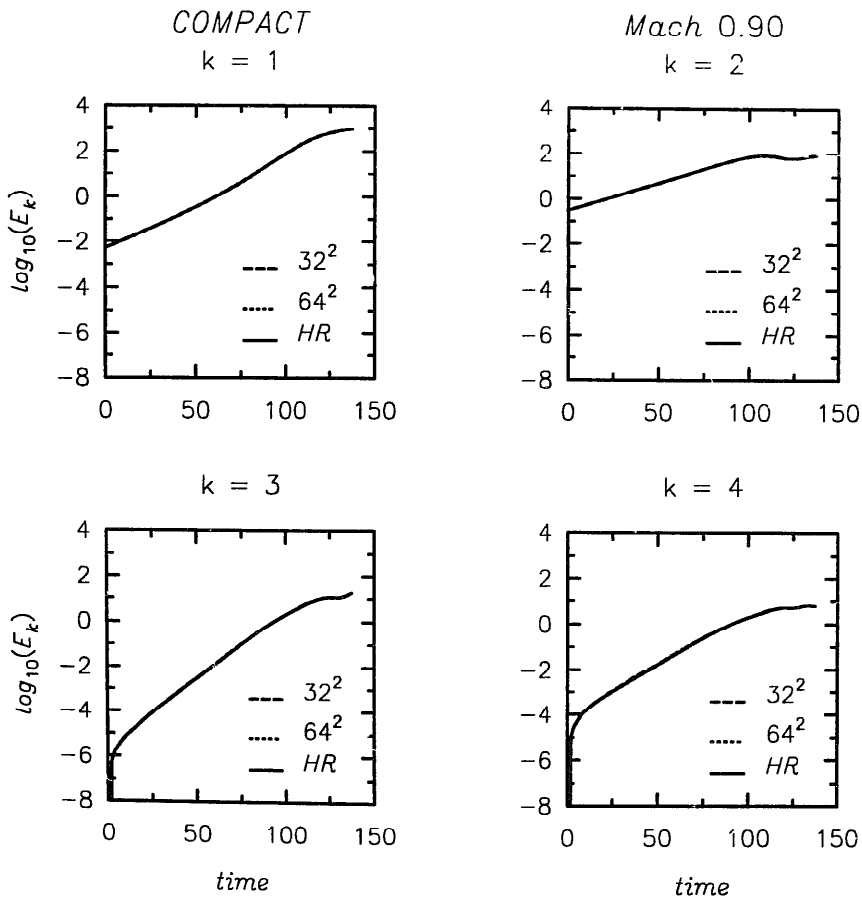

Fig. 12. Evolution of the 4 lowest Fourier harmonics for the Mach 0.9 free shear layer problem using the sixth-order compact scheme.

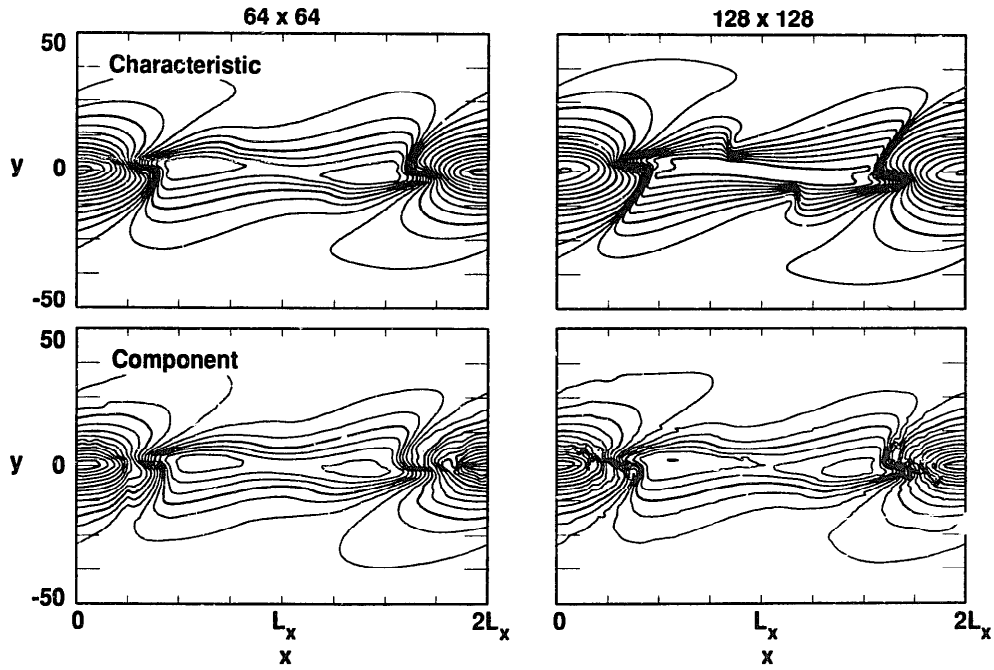

Fig. 13. Pressure field for the Mach 0.9 free shear layer problem at $t = 125$ using the third-order ENO scheme in characteristic form (top) and in component form (bottom). Both 64^2 (left) and 128^2 (right) results are given.

5. Isotropic turbulence

In [15], Passot and Pouquet simulated two-dimensional, compressible, isotropic flows in the turbulence regime using a Fourier spectral collocation method. They identified three basic

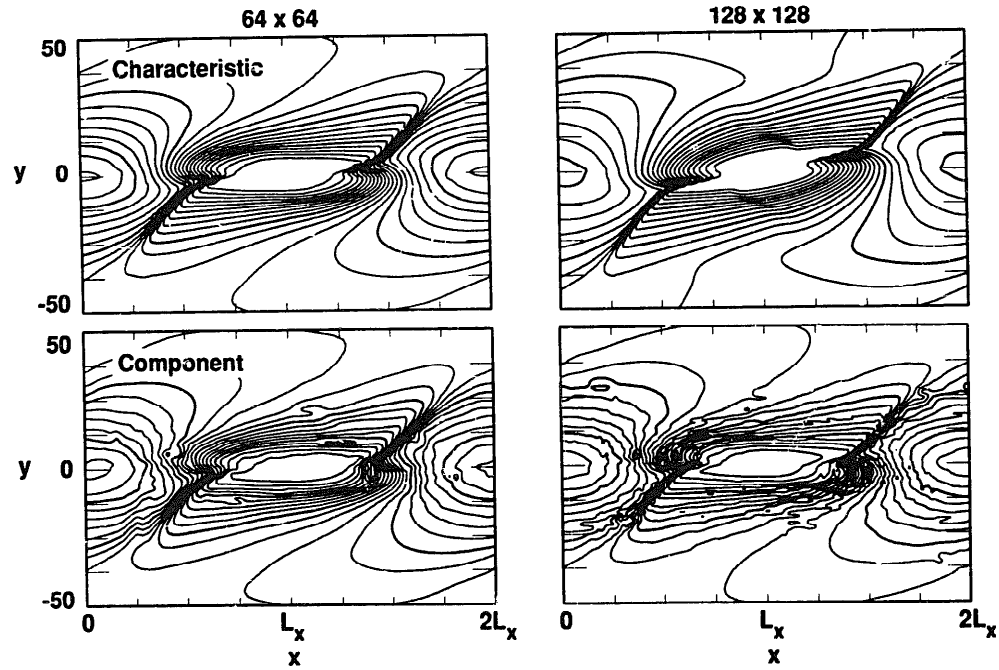

Fig. 14. Pressure field for the Mach 0.9 free shear layer problem at $t = 150$ using the third-order ENO scheme in characteristic form (top) and in component form (bottom). Both 64^2 (left) and 128^2 (right) results are given.

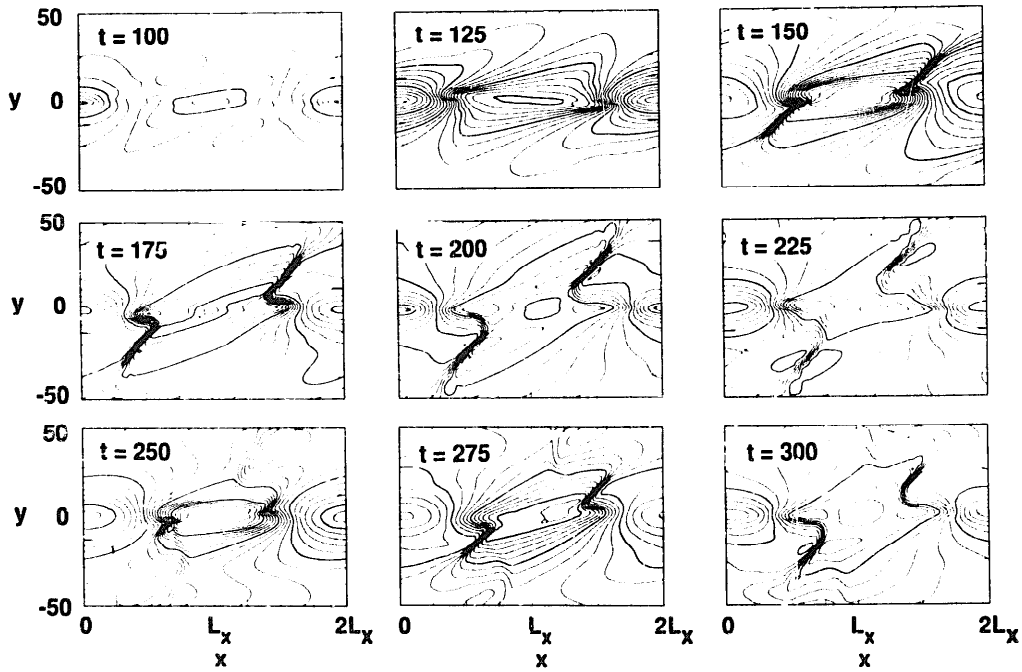

Fig. 15. Pressure field for the Mach 0.9 free shear layer problem from a 64^2 inviscid ENO-2 calculation.

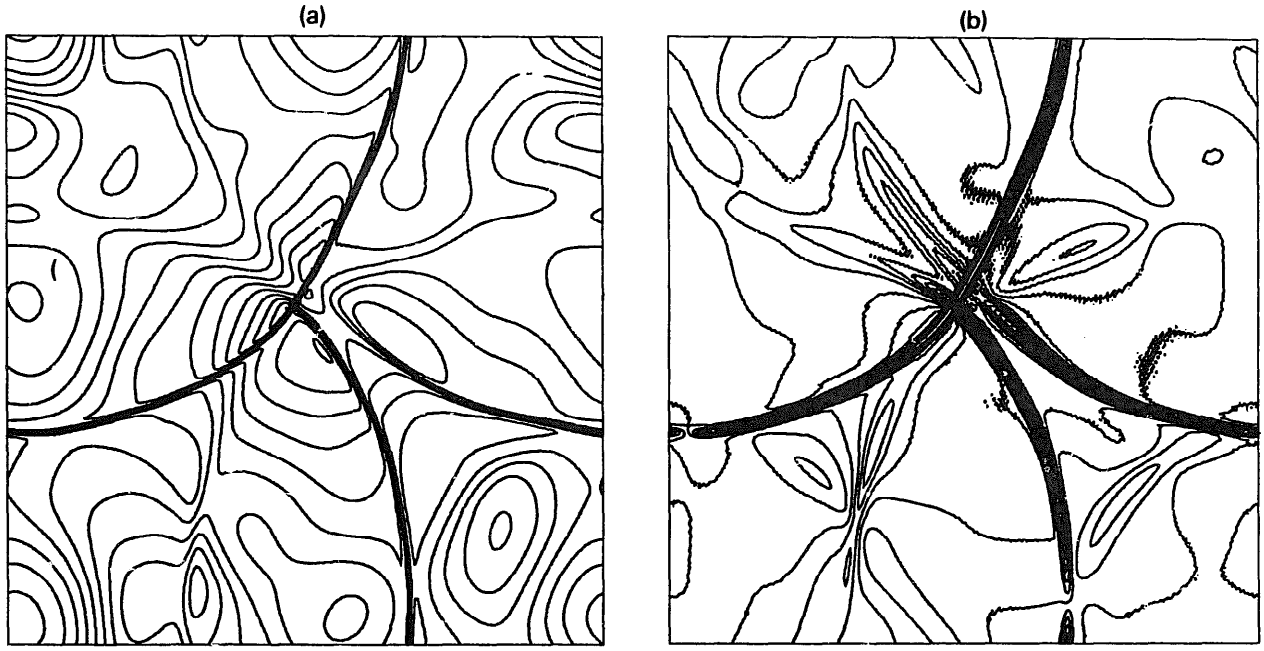

Fig. 16. Density (left) and vorticity (right) contours for the spectral scheme with 256^2 grid points.

regimes: shock-free, weak shocks, and strong shocks. Subsequently, Erlebacher et al. [5] developed a theory of compressible turbulence that contained a more refined characterization of the different regimes of compressible turbulence and contained a useful parametrization of initial conditions that permitted precise predictions of the asymptotic turbulence state. The direct simulations performed in these studies were limited to quite low Reynolds numbers, particularly in the shock regimes. Gibbs oscillations arose whenever the shocks were too thin for the grid to resolve.

Here we perform simulations of compressible isotropic turbulence using both spectral and ENO methods. The boundary conditions are periodic in all directions, the velocity is normalized by its initial root-mean-square value, the density and the temperature are normalized by their mean values, the pressure as for the free shear layer problem, and the viscosity is taken to be constant $\mu = \frac{1}{150}$. We compute a low Mach number case where the shocks are weak and the spectral method can resolve the full structure with 256^2 points. Comparisons between different ENO schemes and between ENO schemes and spectral methods are furnished for both large-scale and small-scale flow features.

In Fig. 16, we show the density and vorticity contours at $t = 1$ computed with the spectral method using 256^2 points. This can be considered to be a resolved solution. Still, the vorticity, which involves derivatives for the numerical solution, shows some oscillations. In Figs. 17 and 18, we show the density and vorticity contours at $t = 1$ for the spectral method and the third-order characteristic ENO-LF, respectively, using 64^2 and 128^2 points. We can see that the ENO scheme produces non-oscillatory results but the spectral method gives noticeable oscillations. For this example, the componentwise ENO-Com produces results similar to those of ENO-LF.

In Figs. 19, 20 and 21, we show the time history of the average Mach number, the maximum Mach number, and the minimum divergence, for the spectral schemes and the third-order ENO-LF. We can see the convergence of ENO schemes for the former two but not the latter.

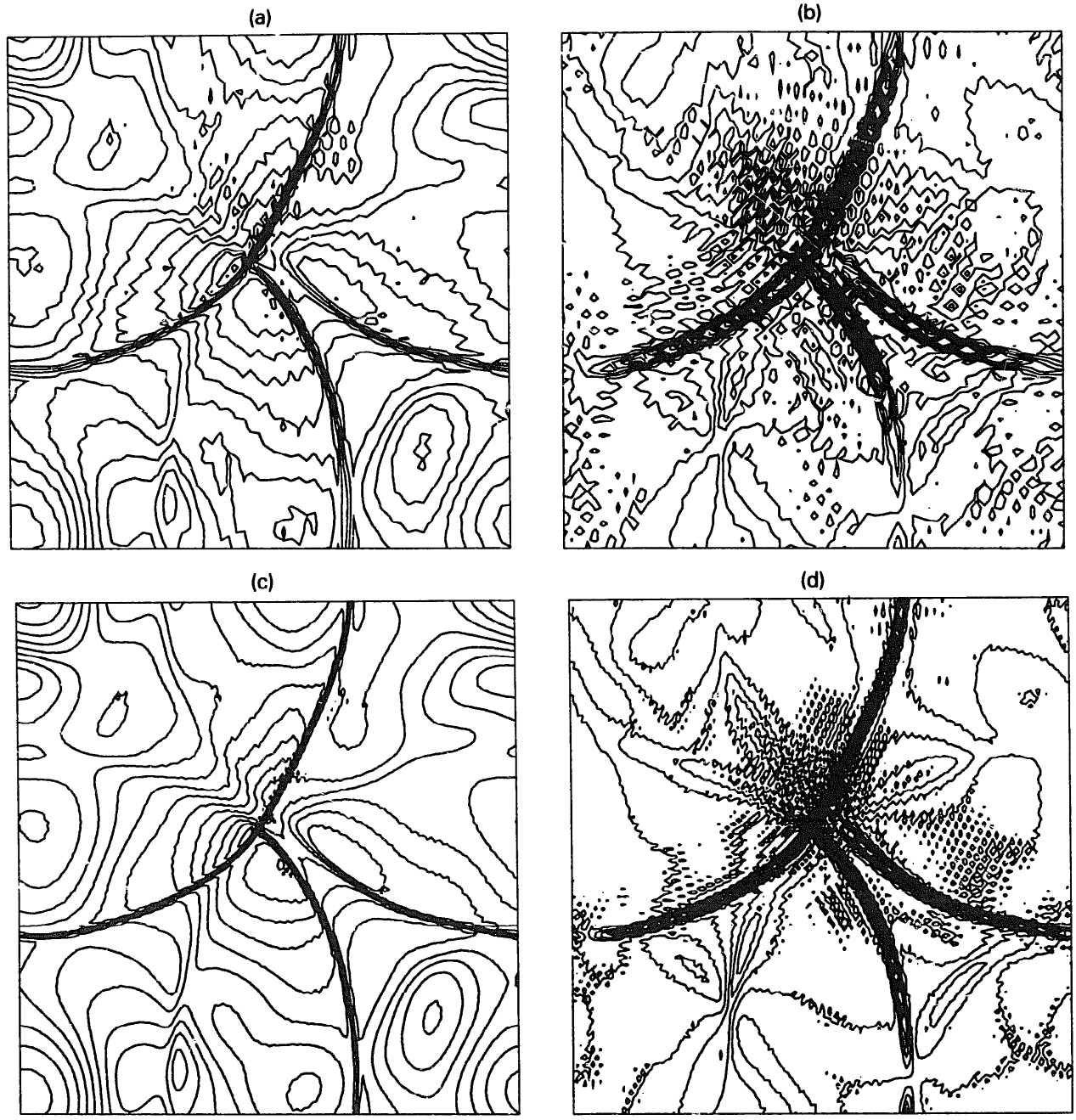

Fig. 17. Density (left) and vorticity (right) contours for the spectral scheme with 64^2 (top) and 128^2 (bottom) points.

In fact minimum divergence is achieved exactly inside the transition regions: to resolve it, one has to resolve the full transition regions. The idea of using high-order shock capturing methods is to resolve essential features in the smooth part of the flow without fully resolving the transition regions or shocks. An important topic of numerical tests is to verify whether this is achieved. For this example we indeed achieve this as indicated by Figs. 19 and 20.

We then compute a three-dimensional version of this problem. We present in Figs. 22, 23, 24 the time history of average Mach number, maximum Mach number and minimum divergence of velocity. These have characteristics similar to their two-dimensional counterparts. The mini-

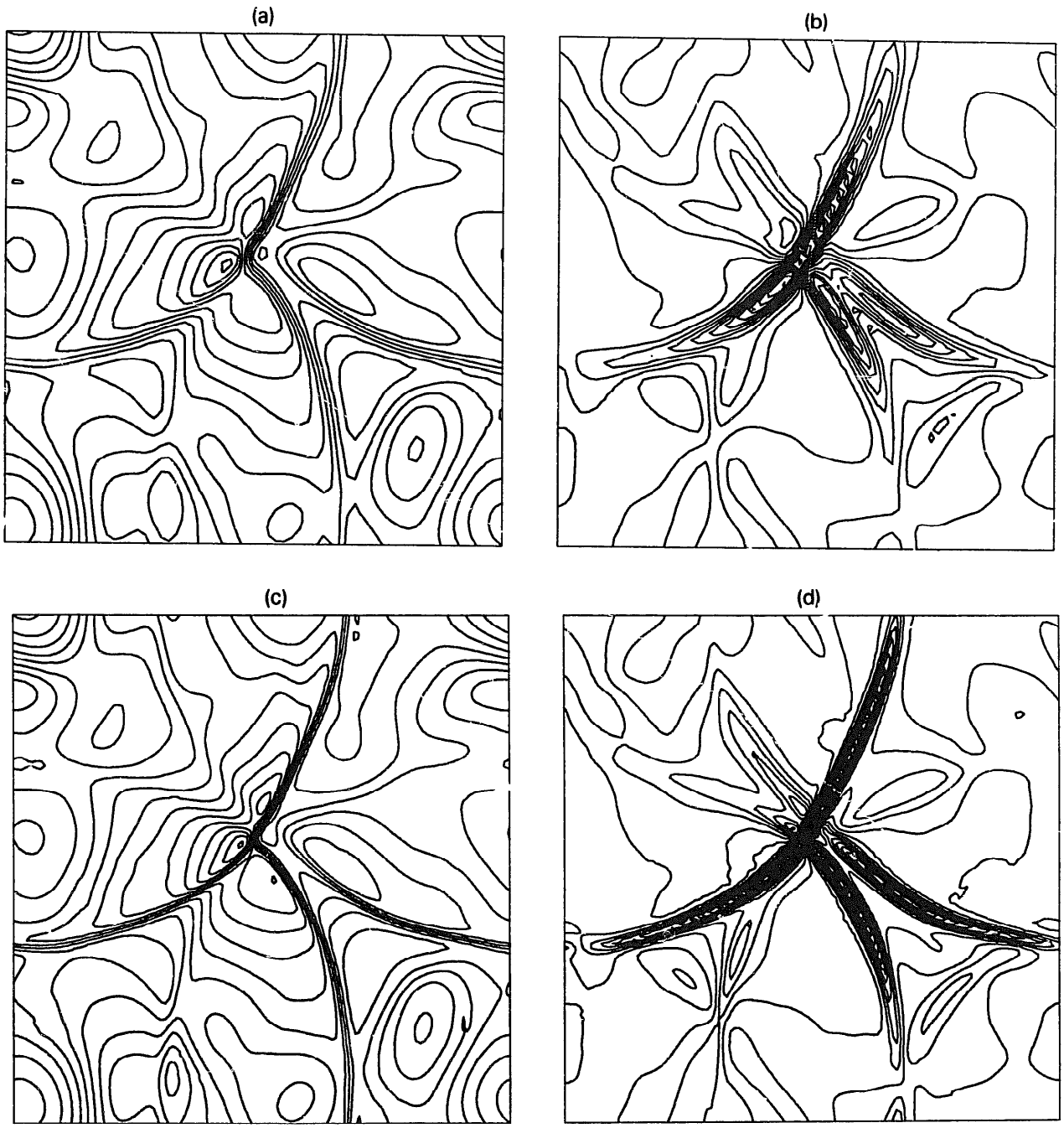

Fig. 18. Density (left) and vorticity (right) contours for the third-order ENO-LF with 64^2 (top) and 128^2 (bottom) points.

mum divergence time history strongly suggests the presence of three-dimensional shocks. However, the grid resolution is not sufficient to clearly bring them out by simple flow visualization.

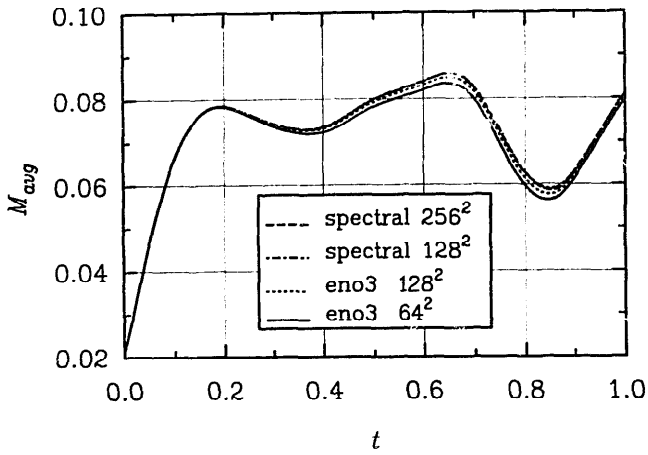

Fig. 19. Time history of average Mach number.

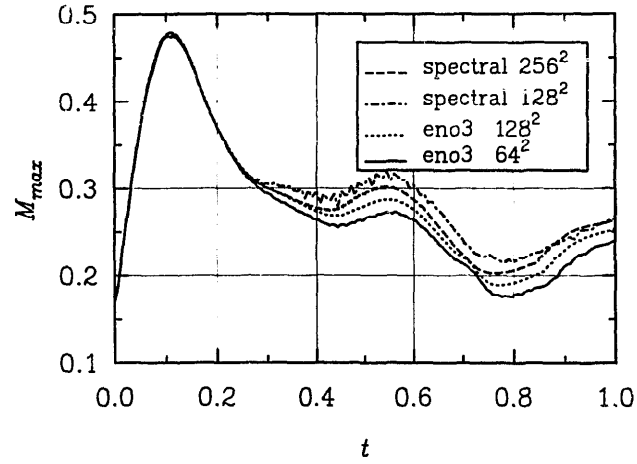

Fig. 20. Time history of maximum Mach number.

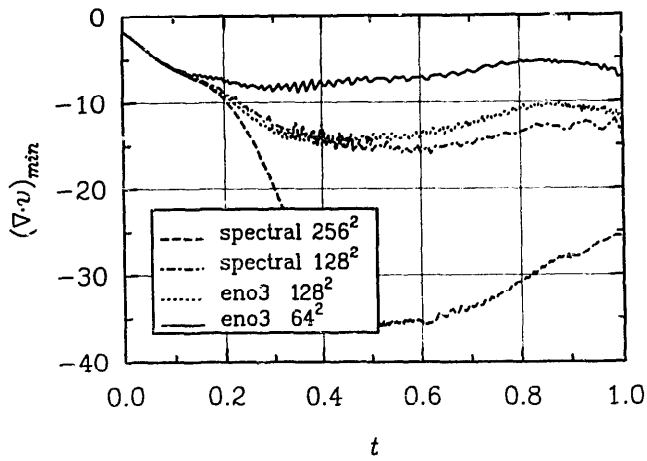

Fig. 21. Time history of minimum divergence.

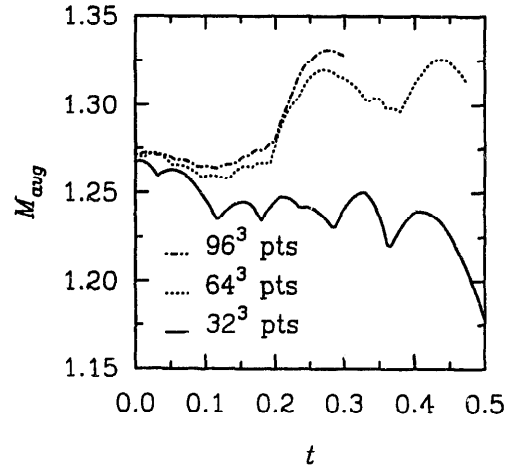

Fig. 22. Time history of average Mach number, 3D.

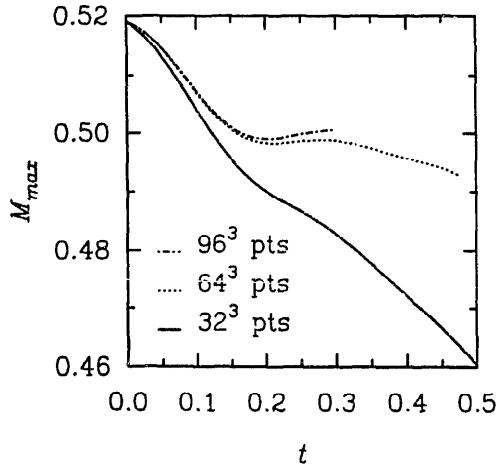

Fig. 23. Time history of maximum Mach number, 3D.

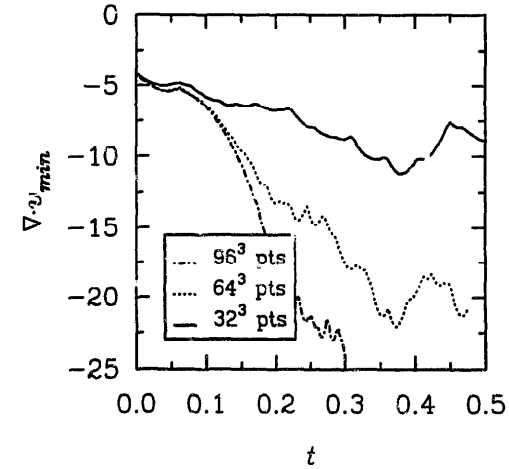

Fig. 24. Time history of minimum divergence, 3D.

6. Shock interaction with entropy waves

For shock interaction with weak entropy and vorticity waves, some qualitative pictures have already been presented in [23, 14], which are similar to those obtained by shock-fitting methods [27]. Here we want to do some quantitative studies of wave amplification factors. This is relevant to the issue raised in Example 1: if the shock or the rapid transition region is not completely resolved, can we still resolve smooth information passing through the shock, such as the amplification factor when waves pass through a shock. For this purpose we take an entropy wave with a small amplitude so that the linear effects dominate and a comparison with linear amplification factor can be made. For third-order ENO with 150×20 grid points (about 20 points per wavelength), we can already resolve the amplitude amplification factor to within 5%. This compares very well against a second-order MUSCL type TVD scheme with the same number of grid points which can only resolve the amplitude amplification factor with an error six to ten times as big. Similar comparisons in the one-dimensional case were also made (via graphs) in [23]. We remark that this quantitative comparison is important in this case, since a major difference between ENO and TVD schemes is that the latter "clips" the critical points. If we only compare contours we will not see such sharp differences.

The details of this problem are as follows. For a pure shock with Mach number M moving to the right, we add an entropy wave

$$\rho = \rho_r \, e^{-(\epsilon_r \cos \beta_r / P_r)}, \tag{34}$$

where $\beta_r = k_r(x \cos \alpha_r + y \sin \alpha_r)$, to the density field at the right of the shock. Here α_r is the angle of the vorticity wave with the shock, k_r controls the number of waves, and ϵ_r is the scaled amplitude. In order to enforce periodic boundary conditions in the y direction, we take the computational domain to be $[0, 1] \times [0, 2\pi/(k_r \sin \alpha_r)]$.

The first phase of this computation is aimed at reducing the transients that arise from the discrete ENO approximation to the moving shock wave. We run the scheme until the shock moves from $x = 0.2$ to $x = 0.8$, then shift the data leftwards so that the shock is again located at $x = 0.2$, and repeat this process six times. Then for each fixed x to the left of the shock, we perform a Fourier analysis on the entropy to find the amplitude ϵ_l, where (34) with the subscripts "r" replaced by "l" denotes the entropy wave to the left of the shock. The resulting amplitude ϵ_l is then averaged over an x-interval between the wave front and the shock, with a length at least one full wavelength.

The computed amplification factors ϵ_l/ϵ_r, together with the linear prediction results, for Mach 3, $\alpha_r = 30°$, $\epsilon_r = 0.02$, $k_r = 15$, are listed in Table 4. The sixth-order ENO method refers

Table 4
Relative errors in amplification factors

Method	$N_x = 50$	$N_x = 100$	$N_x = 150$
2nd-order MUSCL	−86%.	−.6%	−42%
3rd-order ENO	−47%	−14.5%	−6.86%
6th-order ENO	−21%	−8.63%	−4.74%
3rd-order ENO-2	−47%	−5.98%	−1.82%
6th order ENO-2	−8.43%	−6.96%	−2.38%

to a scheme which is sixth-order in space, and third-order (Runge–Kutta) in time, with a reduced CFL number of 0.2. We can observe from Table 4 that, especially for coarse grids, high-order methods indeed produce much more accurate amplification factors than low-order methods. It seems, however, that we cannot reduce the error below a certain threshold around 2%. Again, round-off effects might be playing a role since the amplitude of the wave is far smaller than the shock strength.

7. Concluding remarks

ENO schemes based on fluxes and Runge–Kutta type TVD time discretizations, introduced in [22, 23] are implemented on Cray 2 supercomputers. Vectorization is realized for all inner loops. Currently the code runs 4.5 times slower than the classical centered-difference schemes of the same order: a factor of 2 is due to the upwind flux splitting $f=f^{+}+f^{-}$, another factor of 2 is due to the adaptive stencil process. If characteristic decompositions are used, the CPU time is increased by another factor of 1.7 to 3. General geometry is handled by transformations. Numerical examples include 2D and 3D homogeneous turbulence, shear flows, and shock interaction with vorticity waves. ENO schemes show their advantage when the solution contains both strong shocks and detailed structures: with a relatively coarse grid, where shocks or rapid transition regions are not fully resolved, quantities like minimum divergence cannot be resolved, but the numerical result is still stable and large-scale quantities such as Mach number and amplification factors can be well resolved.

References

[1] H.L. Atkins, Analysis of a second-order-accurate finite-volume method for temporally-growing compressible shear layers, AIAA Paper No. 89-1809 (1989).
[2] M.H. Carpenter, A high-order compact numerical algorithm for supersonic flows, in: K.W. Morton, ed., Lecture Notes in Physics 371 (Springer, New York, 1990) 254.
[3] A.B. Cain, J.H. Ferziger and W.C. Reynolds, Discrete orthogonal function expansions for non-uniform grids using the fast Fourier transform, *J. Comput. Phys.* 56 (1984) 272–286.
[4] G. Erlebacher and M.Y. Hussaini, Numerical experiments in supersonic boundary-layer stability, *Phys. Fluids A* 2 (1990) 94–104.
[5] G. Erlebacher, S. Sarkar, M.Y. Hussaini, and H.O. Kreiss, The analysis and simulation of compressible turbulence, ICASE Report No. 90-15 (1990).
[6] A. Harten and S. Osher, Uniformly high-order accurate nonoscillatory schemes I, *SIAM J. Numer. Anal.* 24 (1987) 279–309.
[7] A. Harten, B. Engquist, S. Osher and S. Chakravarthy, Uniformly high order accurate essentially non-oscillatory schemes III, *J. Comput. Phys.* 71 (1987) 231–303.
[8] A. Harten, Preliminary results on the extension of ENO schemes to two-dimensional problems, *Proceedings International Conference on Hyperbolic Problems*, Saint-Etienne (1986).
[9] M.Y. Hussaini and T.A. Zang, Spectral methods in fluid dynamics, *Ann. Rev. Fluid Mech.* 19 (1987) 339–367.
[10] S.K. Lele, Direct numerical simulation of compressible free shear flows, AIAA Paper No. 89-0374 (1989).
[11] M.G. Macaraeg, C.L. Streett and M.Y. Hussaini, A spectral collocation solution to the compressible stability eigenvalue problem, NASA TP 2858 (1988).
[12] C.D. Munz, L. Schmidt and S. Schöffel, Numerical simulation of the formation of vortex streets in a compressible fluid, in: A. Buckingham, ed., *The Physics of Compressible Turbulent Mixing* (Springer, Berlin, 1990).

[13] S. Osher and S. Chakravarthy, High resolution schemes and the entropy condition, *SIAM J. Numer. Anal.* 21 (1984) 955–984.
[14] S. Osher and C.-W. Shu, Essentially non-oscillatory shock-capturing methods applied to turbulence amplification in shock wave calculations, in: S. Orszag, ed., Lecture Notes in Engineering (Springer, Berlin, 1990).
[15] T. Passot and A. Pouquet, Numerical simulation of compressible homogeneous flows in the turbulent regime, *J. Fluid Mech.* 181 (1987) 441–466.
[16] S.A. Ragab and S. Sheen, Numerical simulation of a compressible mixing layer, AIAA Paper No. 90-1669 (1990).
[17] P. Roe, Approximate Riemann solvers, parameter vectors, and difference schemes, *J. Comput. Phys.* 27 (1978) 1–31.
[18] A. Rogerson and E. Meiburg, A numerical study of the convergence properties of ENO schemes, *J. Sci. Comput.* (to appear).
[19] N.D. Sandham and W.C. Reynolds, Growth of oblique waves in the mixing layer at high Mach number, *Proceedings 7th Symposium Turbulent Shear Flows* (1989).
[20] N.D. Sandham and H.C. Yee, A numerical study of a class of TVD schemes for compressible mixing layers, NASA TM 102194 (1989).
[21] C.-W. Shu, Numerical experiments on the accuracy of ENO and modified ENO schemes, *J. Sci. Comput.* (to appear).
[22] C.-W. Shu and S. Osher, Efficient implementation of essentially non-oscillatory shock-capturing schemes, *J. Comput. Phys.* 77 (1988) 439–471.
[23] C.-W. Shu and S. Osher, Efficient implementation of essentially non-oscillatory shock-capturing schemes II, *J. Comput. Phys.* 83 (1989) 32–78.
[24] M. Soetrisno, S. Eberhardt, J.J. Riley and P. McMurtry, A study of inviscid, supersonic mixing layers using a second-order TVD scheme, AIAA Paper No. 88-3676 (1988).
[25] W. Tang, N. Komerath and L. Shankar, Numerical simulation of the growth of instabilities in supersonic free shear layers, AIAA Paper No. 89-0376 (1989).
[26] T.A. Zang, S.E. Krist and M.Y. Hussaini, Resolution requirements for numerical simulations of transitions, *J. Sci. Comput.* 4 (1989) 197–217.
[27] T.A. Zang, D. Kopriva and M. Hussaini, Pseudospectral calculation of shock turbulence interactions, in: C. Taylor et al., eds., *Numerical Methods in Laminar and Turbulent Flow* (Pineridge Press, Swansea, 1984) 210–221.